Supporting Information

Insulator-to-Metal Transition of Cr_2O_3 Thin Films via Isovalent Ru^{3+} Substitution

Kohei Fujiwara,[*,†] Miho Kitamura,[‡] Daisuke Shiga,[‡,⊥] Yasuhiro Niwa,[‡] Koji Horiba,[‡] Tsutomu Nojima,[†] Hiromichi Ohta,[§] Hiroshi Kumigashira,[‡,⊥] and Atsushi Tsukazaki[†,#]

[†]Institute for Materials Research, Tohoku University, Sendai 980-8577, Japan

[‡]Institute of Materials Structure Science, High Energy Accelerator Research Organization (KEK), Tsukuba 305-0801, Japan

[⊥]Institute of Multidisciplinary Research for Advanced Materials, Tohoku University, Sendai 980-8577, Japan

[§]Research Institute for Electronic Science, Hokkaido University, Sapporo 001-0020, Japan

[#]Center for Spintronics Research Network (CSRN), Tohoku University, Sendai 980-8577, Japan

[*]Author to whom correspondence should be addressed: kfujiwara@imr.tohoku.ac.jp

Table S1. Growth conditions, x values, and t values for some of the $(Cr_{1-x}Ru_x)_2O_3$ films used in this study. The deposition duration was not constant. XRD: X-ray diffraction, E: electrical measurements, M: magnetization measurements, TEM: transmission electron microscopy, PES: photoemission spectroscopy, and XAS: X-ray absorption spectroscopy.

Sample ID	Nominal Ru / Cr ratio in targets	T_g (°C)	Ru content x by SEM-EDX	Thickness t (nm)	Experiment
#1	0	600	0	18	XRD
#2	1.0	600	0.30	23	XRD
#3	1.0	700	0.27	25	XRD, TEM
#4	1.7	670	0.52	43	XRD, TEM
#5	2.0	600	0.57	70	XRD
#6	1.0	800	0.16	16	E
#7	1.0	800	0.21	90	E, M
#8	1.0	700	0.28	60	XRD, E, XAS
#9	1.7	750	0.30	70	E, M
#10	1.7	750	0.34	85	E, M
#11	1.7	735	0.40	80	XRD, E, XAS
#12	1.7	735	0.40	95	E, M
#13	1.7	675	0.47	85	E, M
#14	2.0	720	0.53	70	XRD, E, PES, XAS
#15	0	600	0	117	M

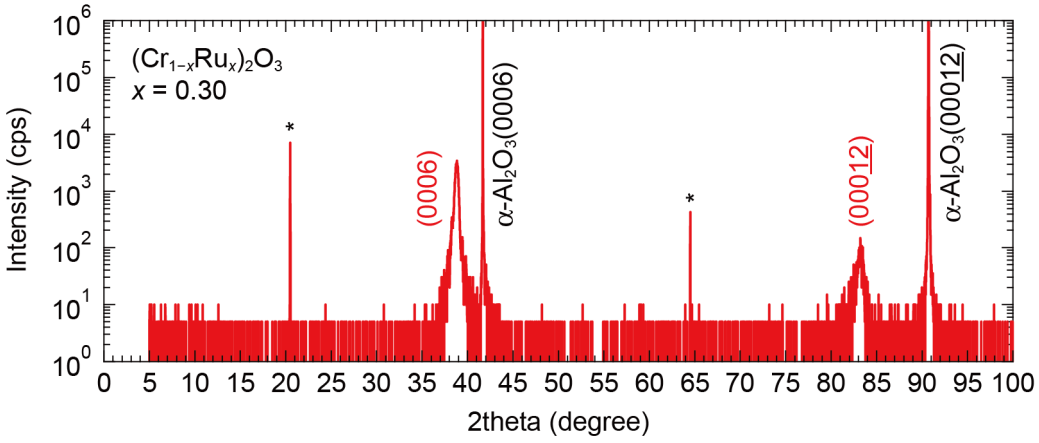

Figure S1. Wide-range out-of-plane XRD pattern for a $(Cr_{0.70}Ru_{0.30})_2O_3$ film (sample #2). The asterisks indicate forbidden reflections of α-Al_2O_3.

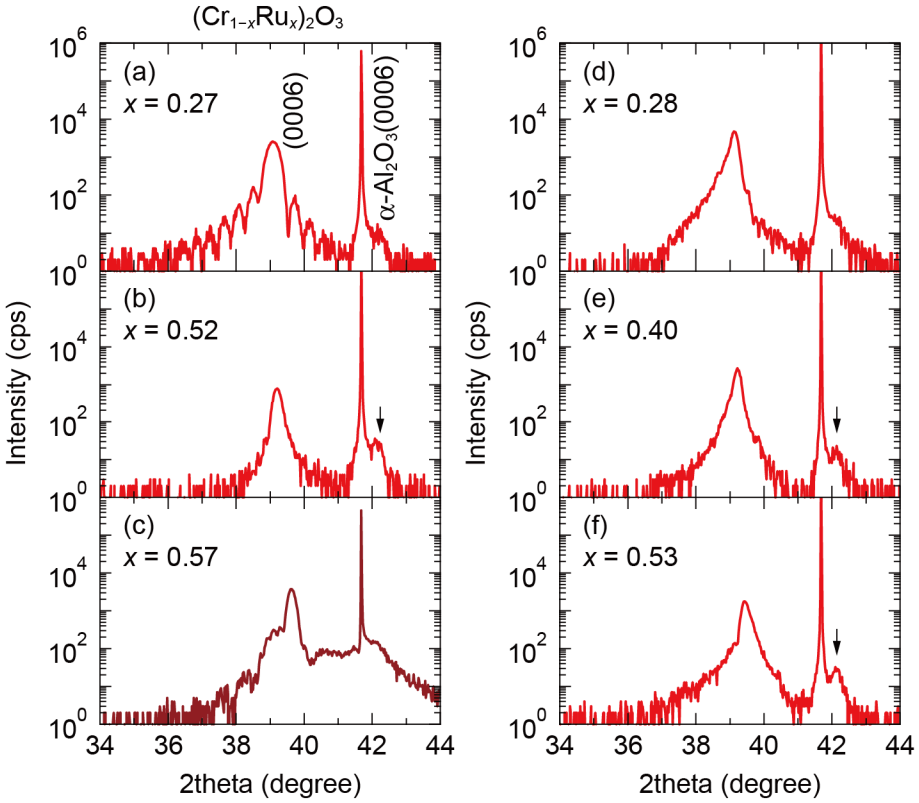

Figure S2. XRD patterns for the $(Cr_{1-x}Ru_x)_2O_3$ films used for (a), (b) TEM analysis in Fig. 2, (c) a solubility limit check, and (d)–(f) spectroscopic measurements shown in Figs. 4 and 5. These films correspond to samples #3, 4, 5, 8, 11, and 14, respectively. With the exception of (c), the films exhibited sharp (0006) diffraction peaks. The arrows indicate an unidentified peak at approximately $2\theta = 42.1°$. The asymmetry of diffraction peak seen in (c), (d), and (f) may reflect the structural inhomogeneity in the films.

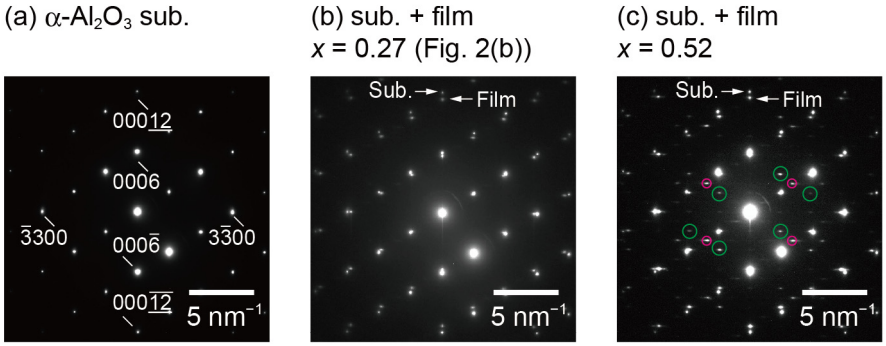

Figure S3. Selected-area diffraction patterns of (a) the α-Al_2O_3 substrate region, (b) the film and substrate regions of a $(Cr_{0.73}Ru_{0.27})_2O_3$ film (sample #3), and (c) the film and substrate regions of a $(Cr_{0.48}Ru_{0.52})_2O_3$ film (sample #4). The data were acquired over an area of ~ a few hundreds of nm in diameter. As indicated by large green circles in (c), diffraction spots corresponding to the inverted domains appear for x = 0.52, consistent with the real-space TEM image in Fig. 2(c). Unidentified diffraction spots indicated by small pink circles might come from precipitates that are often generated in the pulsed-laser deposition process.

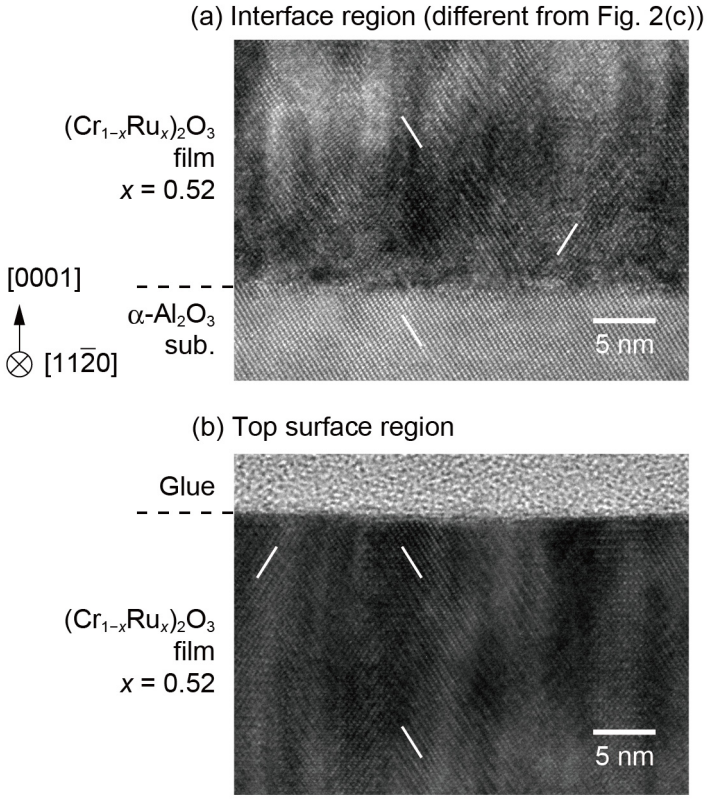

Figure S4. Bright-field TEM images of a $(Cr_{0.48}Ru_{0.52})_2O_3$ film (sample #4) viewed along the $[11\bar{2}0]$ direction: (a) the interface region (different from that shown in Fig. 2(c)) and (b) the top surface region. The $(1\bar{1}02)$ plane characteristic of the corundum-type structure (indicated by slanting white lines) is commonly observed in all regions.

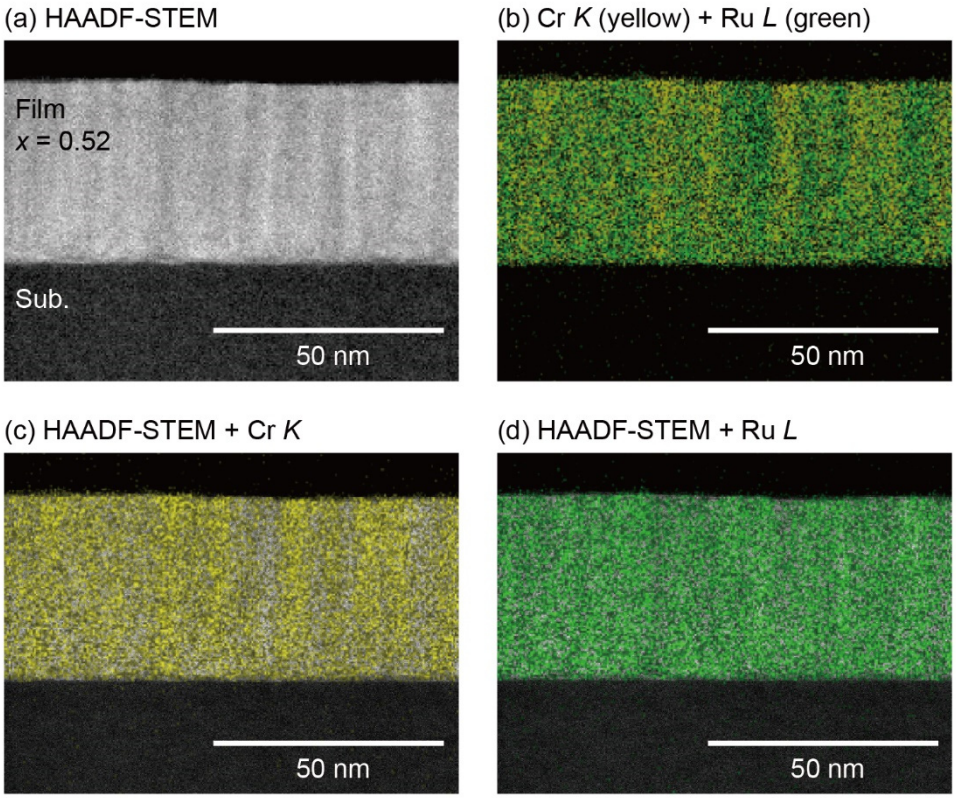

Figure S5. (a) High-angle annular dark-field scanning TEM (HAADF-STEM) image taken for a $(Cr_{0.48}Ru_{0.52})_2O_3$ film (sample #4). Overlaid images of (b) Cr *K* (yellow) and Ru *L* (green) mapping results (count mode), (c) HAADF-STEM and Cr *K*, and (d) HAADF-STEM and Ru *L*. It is clear that the Ru-rich (green) region is not specific to the interface or the top surface of the film.

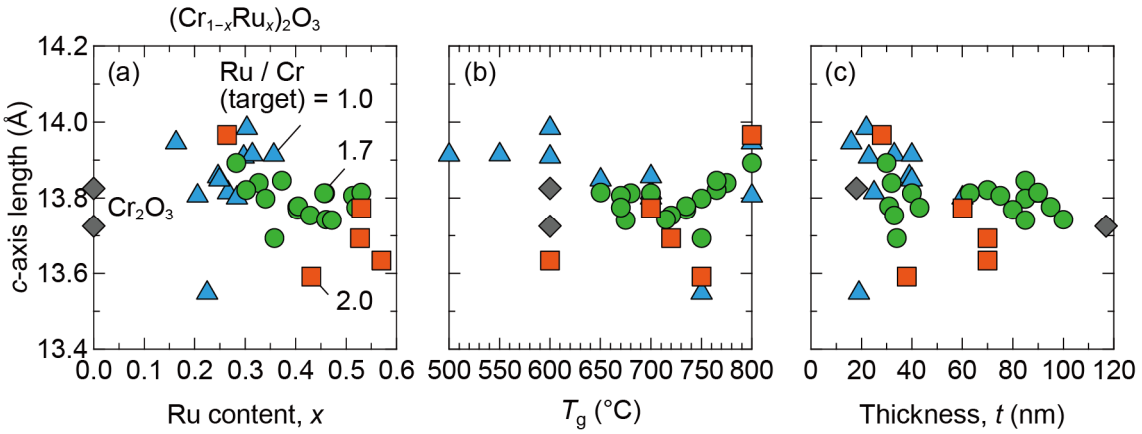

Figure S6. (a) x dependence of c-axis length (c_{XRD}) for $(Cr_{1-x}Ru_x)_2O_3$ films fabricated using targets with nominal Ru / Cr ratios of 1.0, 1.7, and 2.0. The results of non-doped Cr_2O_3 films (samples #1 and 15) are also included for comparison. The c-axis length was calculated from the 2θ values of (0006) XRD peaks by assuming that the films were crystalized in the corundum structure. (b) T_g dependence and (c) t dependence of c-axis length for the same sample set. There are no clear systematic changes in c-axis length as x, T_g, and t vary.

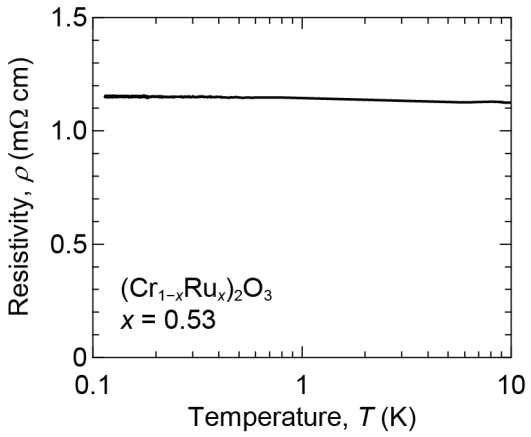

Figure S7. ρ versus T characteristics of a metallic $(Cr_{0.47}Ru_{0.53})_2O_3$ film (sample #14) as evaluated by adiabatic demagnetization refrigerator (ADR) measurements. The XRD pattern is shown in Fig. S2(f).

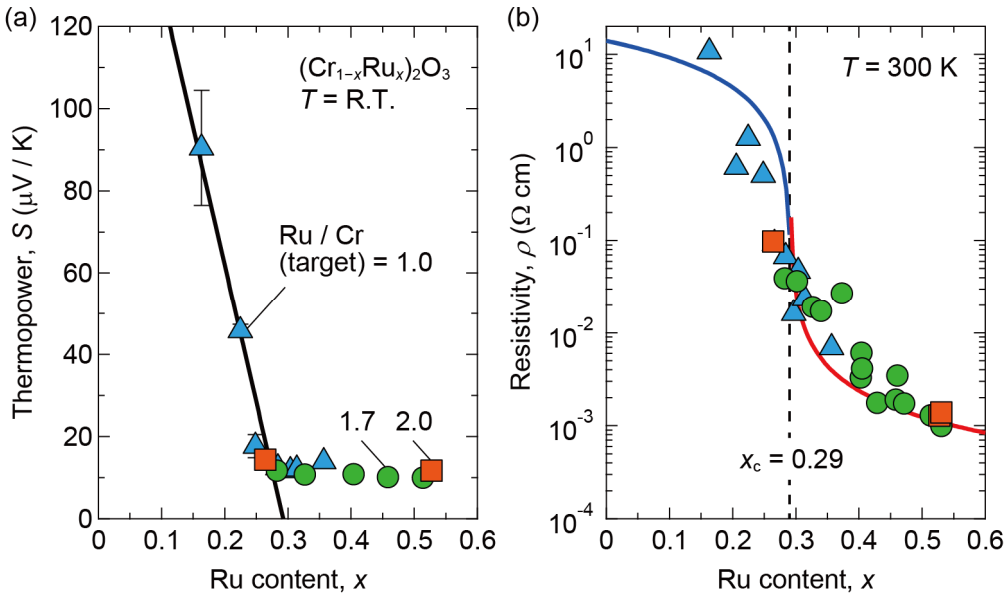

Figure S8. Fitting results for (a) thermopower S and (b) resistivity ρ based on the percolation model[37,38] assuming conducting RuO_2 and non-conducting Cr_2O_3 columnar domains grown perpendicular to the α-Al_2O_3 substrate. The data are the same as those shown in Fig. 3. Calculating a linear fit for the S data in the low-x region (the bold black line in (a)) using Eq. 7 in Ref. 38, we first determined the percolation threshold x_c to be 0.29. Inserting the x_c value into Eq. 5 in Ref. 38, we analytically obtained a fitting curve for ρ below x_c, with ρ (x = 0) of 14 Ω cm, as shown by the bold blue curve in (b). However, this curve does not reproduce the trend of variation in ρ. Furthermore, the fitting parameter of ρ (x = 0) = 14 Ω cm is too low for highly resistive Cr_2O_3 films (x = 0) with $\rho >> 10^3$ Ω cm (as checked by the two-probe method). The bold red curve shows a fitting curve for the ρ above x_c, which also deviates from the ρ data, in particular for $0.30 < x < 0.40$. The actual ρ values seem to decrease more gradually. Judging from these discrepancies, we conclude that the simple percolation model is not adequate for explaining the x dependence of ρ in $(Cr_{1-x}Ru_x)_2O_3$ films.

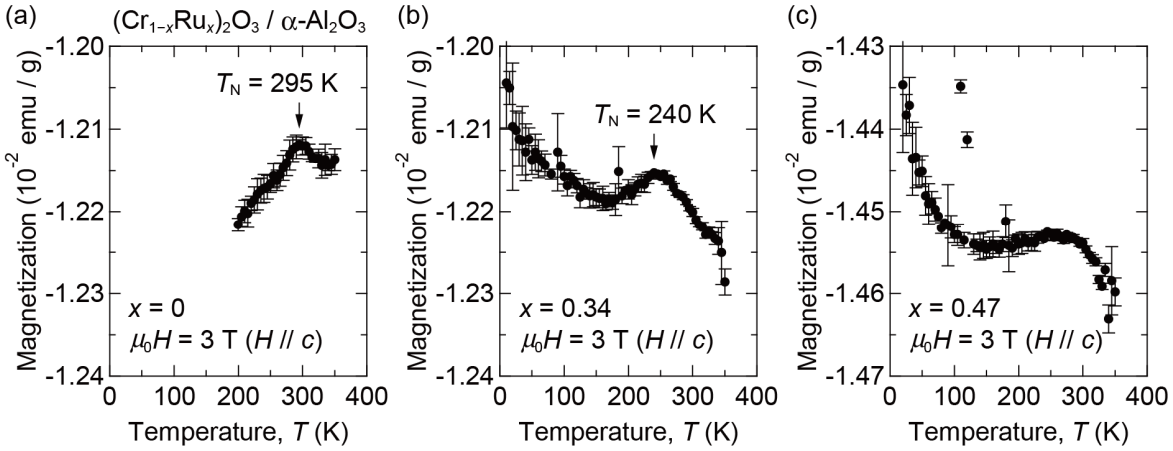

Figure S9. Magnetization versus temperature T curves measured for (a) Cr_2O_3 (sample #15), (b) $(Cr_{0.66}Ru_{0.34})_2O_3$ (sample #10), and (c) $(Cr_{0.53}Ru_{0.47})_2O_3$ (sample #13) films in an out-of-plane magnetic field of μ_0H = 3 T (μ_0 is the vacuum permeability and H is the magnetic field strength). Error bars indicate standard deviations of the data. The magnetization, including a diamagnetic contribution from the substrate, was normalized using the total sample weight (i.e., the total weight of the film and the 0.348 mm-thick α-Al_2O_3 substrate). The total sample weights of samples #15, 10, and 13 were 0.07202 g, 0.06457 g, and 0.06055 g, respectively. The upturns at low T in (b) and (c) were also seen for a bare α-Al_2O_3 substrate that experienced a similar heating process in the PLD chamber. Black arrows indicate local magnetization maximums used for the determination of T_N.

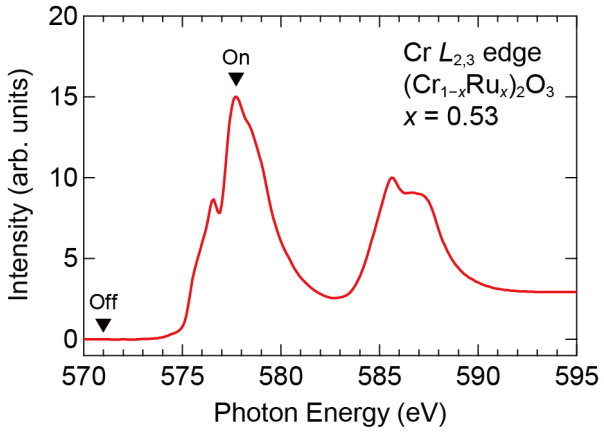

Figure S10. Cr $L_{2,3}$ XAS data measured for a metallic $(Cr_{0.47}Ru_{0.53})_2O_3$ film (sample #14). The spectral features are in excellent agreement with those of Cr^{3+}.[41] On-resonance and off-resonance photon energies for Cr 2*p*-3*d* resonant PES (Fig. 4(b)) are indicated by black triangles.